

# Flexible THz Carrier-Envelope Phase Shifter Based on Metamaterials

Tong Li, Baogang Quan, Guangyou Fang,\* and Tianwu Wang\*

The ability to manipulate terahertz (THz) waveform is important for its applications. Despite rapid progress in metamaterials (MMs), the carrier-envelope phase (CEP) control for THz pulse is still challenging due to its broadband feature. THz scanning tunneling microscope (THz-STM), as an emerging technique combining both high temporal and spatial resolution, imposes additional requirements. Here, an ultra-thin and flexible THz CEP shifter with five groups of different MM arrays is proposed. The CEP shifter is based on a specified split-ring resonator with a pair of cross-oriented gratings to enhance transmission efficiency. Simulation and experimental results show that the CEP of the THz pulse is modulated by passing through different MM arrays in turn, which can be shifted as high as  $2\pi$ . The CEP shifter has good tolerance to wide-angle oblique incidence and structural bending, which is expected to be used as a key component for THz-STM. The structure of the CEP shifter has many potential applications, including THz wave focusing, beam-steering, spatial phase modulation, and structured light generation.

sub-picosecond THz pulse to the nanotip to modulate the bias of the tunnel junction, has achieved atomic resolution on ultrafast timescales.<sup>[8–17]</sup> In order to further manipulate light-field-driven processes in the ultrafast and ultrasmall regime, researchers use the CEP of broadband THz pulse to modulate the potential barrier between the nanotip and sample.<sup>[10,12,15,17]</sup> This strong nonlinear effect is helpful to realize the ultrafast coherent control of electron transport on the atomic scale.<sup>[18–20]</sup> Especially, it is vital to switch the polarity of bias at the STM junction by controlling the CEP of the THz pulse. Therefore, the CEP control techniques of broadband THz pulse are important, which is the primary motivation of this work.

The CEP of ultrashort THz pulse is generally stabilized by the technique of self-referencing or difference-frequency

generation (DFG).<sup>[21,22]</sup> A complex THz setup composed of several THz polarization components has been used to control the CEP, but its insertion loss is very large due to the high Fresnel reflection loss.<sup>[23]</sup> Natural materials with weak dispersion response and small birefringence cannot be easily designed for CEP control of THz pulses with broadband frequency components. By contrast, THz devices made of thin-film optical components are expected to exhibit higher modulation depth and support more compact systems.<sup>[24,25]</sup> Metamaterials (MMs), artificial materials with extraordinary optical properties derived from subwavelength structures, exhibit strong dispersion and anisotropic response to EM waves compared with natural materials.<sup>[26–28]</sup> Up to now, many THz phase modulators have been proposed to realize wavefront engineering, which can be roughly divided into free-space phase modulation (FSPM) and guided-wave phase modulation (GWPM).<sup>[29–33]</sup> The former realizes the phase modulation of free-space waves mainly by the change of EM resonance characteristic of MMs. However, since the amplitude and phase satisfy the Kramers–Kronig (K–K) dispersion relation, the greater the modulation depth of phase, the greater the loss of amplitude. Unlike FSPM, GWPM usually controls the phase in guided wave mode by changing the equivalent propagation constant in the waveguide, but these THz phase shifters still have the problems of small phase modulation range, large loss, and high power consumption. It is a feasible scheme to realize a  $2\pi$  phase shift on the sub-wavelength scale by using the resonant phase and Pancharatnam–Berry phase of scatterers with an anisotropic light response.<sup>[34–36]</sup> In order to completely control the equi-phase surface of EM

## 1. Introduction


The carrier-envelope phase (CEP) of the optical pulse determines the instantaneous electric field intensity of the pulse, which plays an important role in many nonlinear physical processes such as high-harmonic generation (HHG), ionization probability of above-threshold ionization, electron localization in dissociation of the molecule, population transfer, and so forth.<sup>[1–4]</sup> Near single-cycle terahertz (THz) pulse has been generated and applied in many fields.<sup>[5–7]</sup> Recently, the THz scanning tunneling microscope (THz-STM), developed by coupling

T. Li, G. Fang, T. Wang  
GBA branch of Aerospace Information Research Institute  
Chinese Academy of Sciences  
Guangzhou 510700, China  
E-mail: gyfang@mail.ie.ac.cn; wangtw@aircas.ac.cn

B. Quan  
Beijing National Laboratory for Condensed Matter Physics  
Institute of Physics  
Chinese Academy of Sciences  
Beijing 100190, China

B. Quan  
Songshan Lake Material Laboratory  
Guangdong 523808, China

B. Quan  
University of Chinese Academy of Sciences  
Beijing 100049, China

 The ORCID identification number(s) for the author(s) of this article can be found under <https://doi.org/10.1002/adom.202200541>.

DOI: 10.1002/adom.202200541

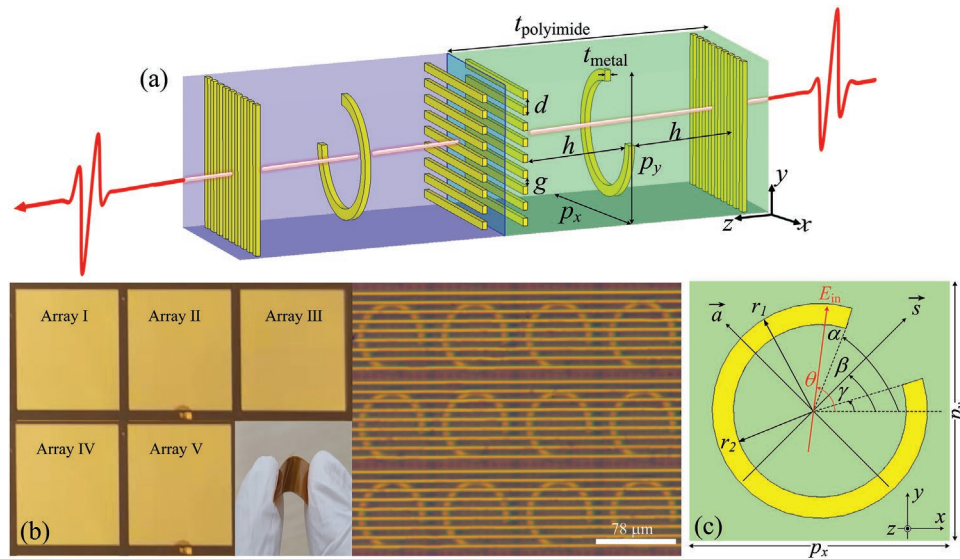


**Figure 1.** Overall and local schematics of the CEP shifter. a) Perspective view of the unit cell of array, which consists of subunit A (pale green area) and subunit B (pale blue area). b) Overall and local optical images of the CEP shifter from the top view, and flexibility of the CEP shifter demonstrated by manually bending the sample. c) Overview of the profile of the SRR in subunit A along the parallel  $x$ - $y$  plane.

waves, these scatterers need to be arranged in arrays. However, these scatterers will change the polarization direction of the incident electric field, and the radiation efficiency is still low. MMs, which can provide both CEP shift and low insertion loss for broadband THz pulse without changing the polarization of the electric field, have not been reported.

In this letter, we realize broadband THz CEP control with MM arrays of different parameters, as shown in **Figure 1**. The unit cell of each array consists of two subunits. One induces an approximately equivalent phase shift over the whole spectrum range, and the other converts the modulated cross-polarized waves back to co-polarized waves. The sample was fabricated using conventional UV lithography, electron beam deposition, and lift-off techniques on polyimide film. The performances of the as-fabricated sample were then characterized using a THz time-domain spectroscopy (THz-TDS) system. Simulation and experimental results show that THz CEP can be ideally adjusted by the proposed MM arrays. Compared to the complex THz CEP controller composed of different parts, the proposed CEP shifter is ultra-thin, flexible, with low insertion loss, and easy to install and operate, which can realize  $2\pi$  shift of CEP in sub-wavelength thickness, as shown in **Table 1**.

## 2. Design and Fabrication

The unit cell of each array consists of subunit A (pale green area) and subunit B (pale blue area), as shown in **Figure 1a**.

**Table 1.** Comparison to reported THz-CEP shifter.

| Ref.      | Bandwidth | Insertion loss  | Thickness                   | Angular robustness | Polarization dependence |
|-----------|-----------|-----------------|-----------------------------|--------------------|-------------------------|
| [23]      | 2.0 THz   | $\approx 10$ dB | $> 87$ nm                   | Weak               | Linear                  |
| This work | 1.6 THz   | $< 4$ dB        | $\approx 160$ $\mu\text{m}$ | Strong             | Linear                  |

In subunit A or B, the orthogonal gratings and split-ring resonator (SRR) made of gold are embedded in a dielectric film made of polyimide. In order to simplify the fabrication process and facilitate the separation or combination of subunit A and subunit B, the two are bonded with silica gel. For subunit A of different arrays, the same structural parameters are  $t_{\text{polyimide}} = 80$   $\mu\text{m}$ ,  $t_{\text{metal}} = 0.2$   $\mu\text{m}$ ,  $d = 8$   $\mu\text{m}$ ,  $g = 4$   $\mu\text{m}$ ,  $h = 30$   $\mu\text{m}$ , and  $p_x = p_y = 38$   $\mu\text{m}$ . The fabricated flexible thin-film CEP shifter consists of five arrays with an area of  $100$   $\text{mm}^2$  for each array, as shown in **Figure 1b**. **Figure 1c** shows the profile of the SRR in subunit A along the parallel  $x$ - $y$  plane, and the corresponding parameters are listed in **Table 2**. For subunit B, it has the same structural parameters as subunit A except for being rotated by  $\pi$  with respect to the  $y$ -axis. Subunit A of different arrays converts the incident co-polarized ( $x$ -polarized) wave into a transmitted cross-polarized ( $y$ -polarized) wave, and modulates the phase of the transmitted wave with SRR of different geometric parameters, thus introducing a different phase for different arrays. Subunit B of different arrays converts the cross-polarized wave back into a co-polarized wave. Since the structural parameters of subunit B of different arrays are exactly the same, no phase difference will be introduced for different arrays. When subunit A and B are bonded together by silica gel, only the CEP of the incident pulse will be modulated, as shown in **Figure 1a**.

**Table 2.** Geometric parameters of SRR.

| Array No.               | I            | II           | III           | IV          | V          |
|-------------------------|--------------|--------------|---------------|-------------|------------|
| $\alpha$                | $72.5^\circ$ | $35^\circ$   | $-17.5^\circ$ | $125^\circ$ | $74^\circ$ |
| $\beta$                 | $45^\circ$   | $-45^\circ$  | $-45^\circ$   | $45^\circ$  | $45^\circ$ |
| $\gamma$                | $17.5^\circ$ | $-125^\circ$ | $-72.5^\circ$ | $-35^\circ$ | $16^\circ$ |
| $r_1$ [ $\mu\text{m}$ ] | 30.5         | 33.5         | 30.5          | 33.5        | 30.5       |
| $r_2$ [ $\mu\text{m}$ ] | 24.5         | 29.5         | 24.5          | 29.5        | 24.5       |

In the THz band, the birefringence coefficient of natural crystal materials is usually not large enough, so it is necessary to increase the device thickness for a large phase delay, which cannot be used in small integrated devices. Different from the gradual accumulation of phases in traditional optical elements, arbitrary phase delay can be realized at the sub-wavelength scale by the strong coupling between EM wave and metasurface.<sup>[29,34-36]</sup> Here, the SRR which reveals a strong response to the THz radiation is the basic unit, as shown in Figure 1c. SRR is one of the simplest anisotropic resonators under certain conditions.<sup>[35]</sup> It is similar to V-shaped antennas but can be designed to be more subwavelength. When the linearly polarized wave is coupled with SRR, the incident electric field component polarized parallel and perpendicular to the symmetry axis of SRR excites the symmetric and antisymmetric eigenmodes of SRR, respectively. For arbitrary incident  $\theta$ -polarized wave, both eigenmodes are excited at the same time, and the scattered field can be expressed as:

$$E_{sca} = \frac{(S+A)}{2} [\cos(\theta)\bar{x} + \sin(\theta)\bar{y}] + \frac{(S-A)}{2} [\cos(2\beta - \theta)\bar{x} + \sin(2\beta - \theta)\bar{y}] \quad (1)$$

where  $S$  and  $A$  denote the complex scattering amplitudes from the symmetric and anti-symmetric modes,  $\bar{x}$  and  $\bar{y}$  are the unit vectors along the  $x$ - and  $y$ -axes, respectively. Obviously, the scattered field contains two terms, which are polarized along the  $\theta$ -direction and the  $(2\beta - \theta)$ -direction from the  $x$ -axis, respectively. For the  $\theta$ -polarized component, that is, the co-polarized wave, it has a phase response similar to that of the incident field but with different amplitudes. Therefore, it is difficult to directly realize large phase delay for co-polarized waves by adjusting the structural parameters of SRR. For the  $(2\beta - \theta)$ -polarized component, its phase delay can easily cover  $0-2\pi$  by changing the structural parameters of the SRR. In our simulation and experiment, the symmetry axis of the SRR is along  $\beta = \pi/4$  and the incident polarized wave is the  $x$ -polarized wave,  $E_{sca} = (S+A)\bar{x}/2 + (S-A)\bar{y}/2$ .

However, due to the bidirectional radiation of electric dipole, SRR has significant reflection and polarization loss, and the polarization conversion ratio (PCR) of SRR does not exceed 25%.<sup>[35]</sup> Therefore, we use multi-beam interference to improve the PCR of SRR, as shown in Figure 2. For metal grating, due to the low-frequency EM Lorentz interaction, the EM mode perpendicular to the metal grating can be transmitted with low loss, while the EM mode parallel to the metal grating will be reflected.<sup>[37]</sup> Therefore, for interface 1 and interface 3, we approximately consider their transmission coefficients  $|t_1^x| = |t_3^x| \approx 1$  and reflection coefficients  $|r_1^y| = |r_3^y| \approx 1$  with  $\pi$  phase change. It should be noted that this approximation is not applicable in higher frequencies. Since the Jones matrix of SRR with mirror plane  $\pi/4$  inclined has equal off-diagonal elements,<sup>[38]</sup> the complex transmission and reflection coefficients of the interface 2 have the following relationship:  $t_2^x = t_2^y, r_2^x = r_2^y, t_2^{yx} = t_2^{xy} = r_2^{yx} = r_2^{xy}$ , where superscript  $x(y)$  represents  $x(y)$ -polarized input and  $x(y)$ -polarized output,  $xy(yx)$  represents  $y(x)$ -polarized input and  $x(y)$ -polarized output. The subscript number represents the interface where the corresponding metal layer is located. The spacer layer is a homogeneous medium that can only provide the phase factor of EM wave propagation. In addition, the thickness of the spacer layer is much greater than that of the metal layer, so the interaction between the metal layers can be ignored. First, the system composed of interface 1, interface 2, and the medium between them is regarded as resonator cavity 1, the complex transmission coefficients can be deemed as the superpositions of multiple reflections and transmissions at the two interfaces:

$$t_{c1}(x) = t'_{c1}(x) + t''_{c1}(x) + \dots = \frac{a^2 t_2^y e^{ikh} - a(t_2^{yx})^2 e^{i3kh}}{b} \quad (2)$$

$$t_{c1}(y) = t'_{c1}(y) + t''_{c1}(y) + \dots = \frac{t_2^{yx} e^{ikh} [b + (t_2^y e^{i2kh})^2 - a t_2^y e^{i2kh}]}{b} \quad (3)$$

where  $k = 2\pi f/c$  is the propagation constant,  $n$  denotes the refractive index of polyimide,  $c$  is the speed of light in free space, and  $f$  is frequency,  $a = 1 + r_2^y e^{i2kh}$ ,  $b = (1 + r_2^y e^{i2kh})^2 - (t_2^{yx} e^{i2kh})^2$ .

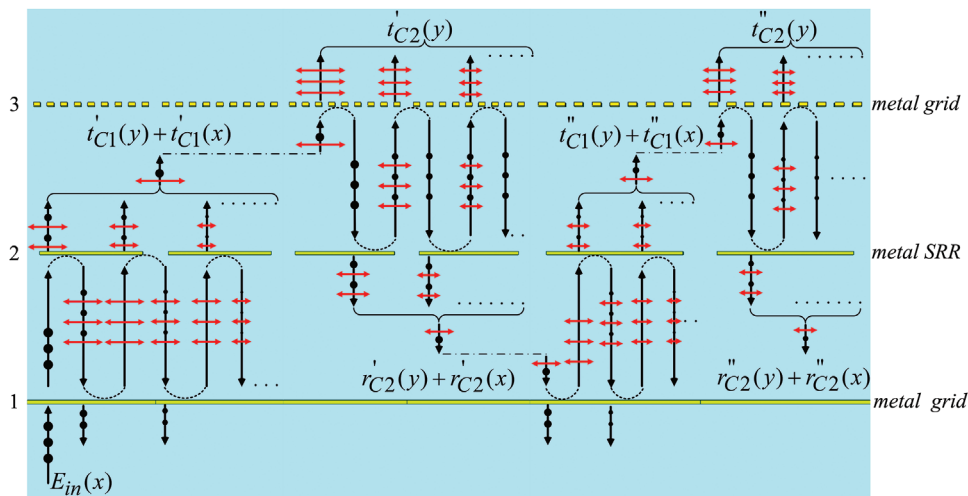


**Figure 2.** Schematic of multiple-beam interference in the thin film composed of subunit A, which shows how multiple reflections and transmissions at the interface affect the transmission and reflection coefficients.

Then, the system composed of interface 2, interface 3, and the medium between them is regarded as resonant cavity 2. Thus, the total complex transmission coefficient can be given as:

$$t_{C2}(y) = t'_{C2}(y) + t''_{C2}(y) + \dots = t_{C1}(y)t_3^y e^{ikh} + t_{C1}(x) \frac{t_3^x t_2^y t_3^y e^{i3kh}}{1 - r_2^x r_3^x e^{i2kh}} \quad (4)$$

$$= \frac{t_2^{yx} e^{i2kh} (1 + r_2^y e^{i2kh} - t_2^y e^{i2kh})^2}{(1 + r_2^y e^{i2kh})^2 - (t_2^x e^{i2kh})^2}$$

Taking the geometric parameters of subunit A in array I as an example, **Figure 3a** shows transmission and PCR as a function of frequency. By comparing the transmission curves of theoretical calculation and simulation, it can be found that they agree well in the range of 0.4–1.6 THz. The difference between them may be due to the neglect of the influence of interlayer coupling in theoretical calculation. The difference between experimental and simulation results may be caused by the dimensional error of microfabrication processes and the change in the dielectric refractive index. In order to understand why transmission decreases at some frequencies and the broadband spectrum response of SRR, we set up a field monitor to monitor the surface current distribution of SRR at 0.67, 1.2, and 1.7 THz, respectively. Obviously, the typical inductance-capacitance (*LC*) resonance (mode I) and the third-order resonance (mode III) are induced by the antisymmetric eigenmode of SRR, and the dipole resonance (mode II) is excited by the symmetric eigenmode of SRR. These three modes reveal discrete resonance behavior and the superposition between them results in a broad spectrum response of SRR. The simulated and measured PCRs show that the PCR of the sample is greater than 90% in the range of 0.4–1.8 THz, which is much higher than the PCR of SRR. Therefore, the PCR of the sample can be

significantly improved by introducing a pair of cross-oriented gratings. The sample was fabricated by a traditional microfabrication process, and its process chart is shown in **Figure 3b**.

### 3. Results and Discussion

Subunits A and B need to be used together to adjust the THz CEP while keeping the polarization unchanged. Since the structures of subunits A and B are the same, only one subunit was investigated with the Finite Integration Technique (FIT). Five groups of special CEP values were designed and fabricated for special applications.<sup>[8–17]</sup> **Figure 4a** shows the simulation results of transmitted far-field THz temporal waveforms with cross-polarization after subunit A in different arrays. Obviously, when the incident pulse is modulated by different arrays in turn, the CEP shift is clearly observed. There is no temporal delay between these pulses, and the envelope (gray dotted line) and duration of the pulse remain unchanged. **Figure 4c** shows the phase shift spectra obtained by the Fourier transformation (FT) of the temporal waveforms, and the results show that phase shift between different arrays is relatively constant in the range of 0.5–1.8 THz when the CEP of array III is set as the reference value. For example, when array III is switched to array I, the shift of CEP of the cross-polarized pulse is  $\pi$ , which realizes the reversal of the signs of the temporal waveform. By carefully designing the geometric parameters of SRR, arbitrary CEP values between 0 and  $\pi$  can be obtained, as shown in **Figure 4e**, which illustrates the CEP shift in the range of  $\pi$  with nearly constant transmission at 1.0 THz. A commercial THz-TDS system is used to observe the CEP shift for different MM arrays in the sample. Since the detector of the THz-TDS

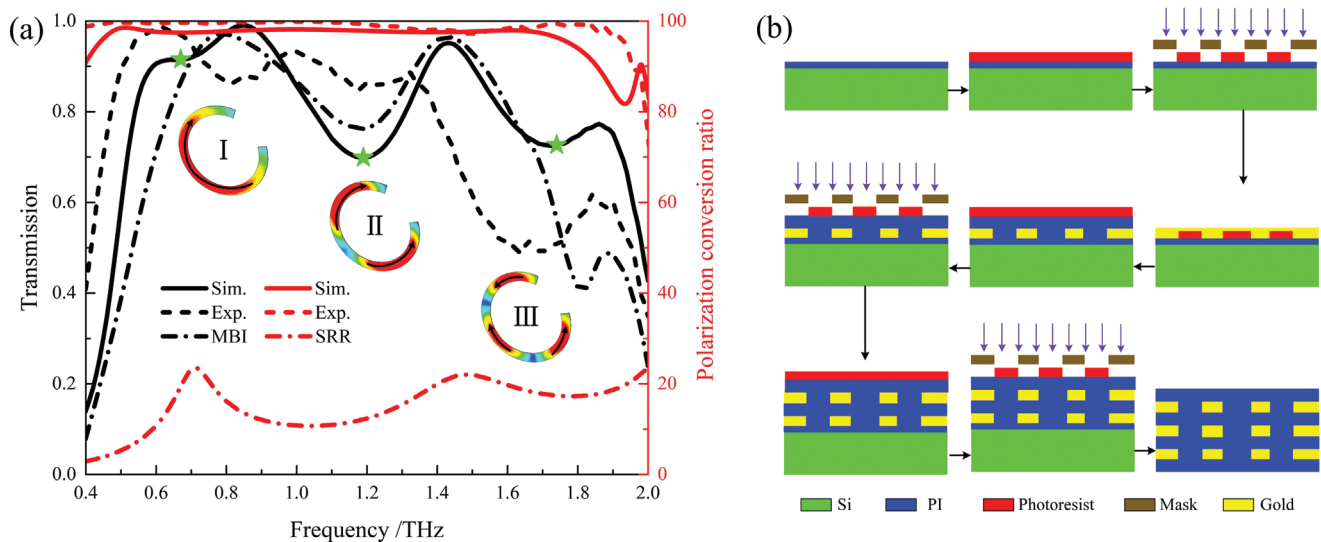


**Figure 3.** a) The transmission and PCR as a function of frequency. Insets: surface current distribution at 0.67, 1.2, and 1.7 THz, respectively. b) The specific illustration of fabrication procedures. In the first step, a polyimide multilayer thin film of 30  $\mu\text{m}$  is prepared onto a silicon wafer using a spin-coating method. Then, 1 mL of image reversal photoresist AZ 5214 E is spin-coated onto the surface of the substrate. Thereafter, the first layer of MMs (metal gratings) is fabricated using conventional UV lithography, electron beam deposition, and lift-off techniques. A second polyimide multilayer thin film of 30  $\mu\text{m}$  as a spacer is prepared onto the first layer of metal gratings. The SRR layer is obtained by a high-precision alignment UV lithography and metal deposition and lift-off process. A third polyimide multilayer thin film of 30  $\mu\text{m}$  as a spacer is prepared onto the SRR layer of metal gratings. A second layer of metal grating, which is perpendicular to the first layer of metal grating, is fabricated by alignment UV lithography and metal deposition and lift-off process. Finally, a top layer of polyimide thin film of 30  $\mu\text{m}$  is prepared to form the flexible MM.

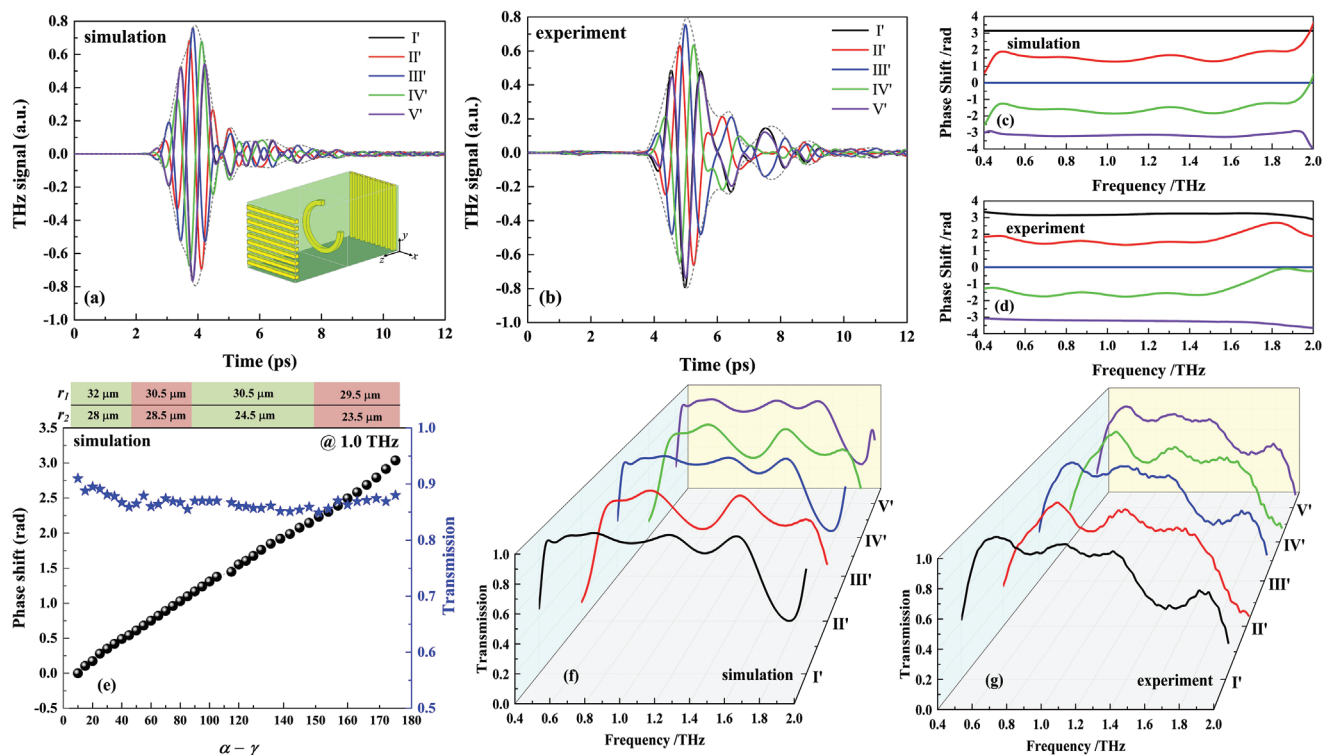


**Figure 4.** Temporal waveforms, phase shift, and transmission spectra of cross-polarized waves. a) Simulated temporal waveforms, where the gray broken lines are the envelope of the THz pulse. Insets: the unit cell of the array, which consists only of subunit A. b) Measured temporal waveforms. c,d) Phase shift spectra obtained by FT of temporal waveforms shown in (a) and (b), respectively. e) Transmission and phase shift as a function of geometric parameters of SRR. f,g) Transmission spectra obtained by FT of temporal waveforms shown in (a) and (b), respectively.

is polarization sensitive, it is necessary to rotate the detector to the cross-polarized direction. Figure 4b,d shows the measured THz temporal waveforms and the phase shift spectra, which are in good agreement with the simulation results. The difference between them is caused by a small mismatch between the fabricated real device and the simulated structure. The simulated and measured transmission spectra are also plotted in Figures 4f and 4g, respectively. The results show that the sample can maintain efficient transmission when modulating the CEP of cross-polarized pulses, the reduction of the transmission for some frequency components is due to the resonant absorption of SRR.

The tolerance of the performance for the incidence angle and sample bending was also checked. First, we simulated and measured the response of the sample at different incidence angles. As shown in Figure 5a,b, the simulation and experimental results show that when the azimuth  $\varphi$  changes from  $0^\circ$  to  $52^\circ$ , the transmission of the sample in the range of 0.4–1.6 THz is almost unaffected, except that the dip with the center frequency near 2.0 THz has a small redshift, indicating good tolerance to the misalignment problems. In addition, polyimide film has good mechanical strength, and its bending strength is greater than 200 MPa at room temperature. Since our sample thickness is only about 100  $\mu\text{m}$ , it's necessary to understand the effect of sample bending on device performance. Next, we checked the sample bending-induced transmission response. In the simulation, when the curvature  $K$  is greater than  $0.06 \text{ mm}^{-1}$ , the transmission appears obvious

absorption around 0.9 and 1.3 THz, as shown in Figure 5c. This is because the structure of the model is complex at this time, and only appropriate sparse mesh to meet the calculation requirements, resulting in poor convergence of the calculation results. As shown in Figure 5d, the experimental results show that when the curvature  $K$  (reciprocal of the radius of the osculating circle) is less than  $0.12 \text{ mm}^{-1}$ , the transmission is not affected by bending in the range of 0.4–1.6 THz, indicating good tolerance to the bending problems. The results of the above experiments show that the fabricated sample shows good robustness in practical application.

For some practical applications, like in THz-STM, the polarization of the THz pulse needs to remain the same while adjusting the CEP. We have demonstrated that the sample composed of subunit A can efficiently modulate the CEP of cross-polarized waves. Since the sample is composed of reciprocity materials, the Lorentz reciprocity condition is satisfied.<sup>[39]</sup> According to the Lorentz reciprocity theorem, if we send the cross-polarized waves modulated by subunit A back to subunit A in the opposite direction, the incident cross-polarized waves will be restored to the transmitted co-polarized waves. Therefore, subunit A was rotated  $\pi$  along the  $\gamma$ -axis to obtain subunit B, which was then combined with subunit A to realize the direct modulation of CEP of the incident pulse. The geometric parameters of subunit B of each array are set the same as those of subunit A of array I to ensure that no additional phase shift is generated between each array. Figure 6a,b shows simulated and measured far-field THz temporal waveforms, respectively. As expected, the introduction

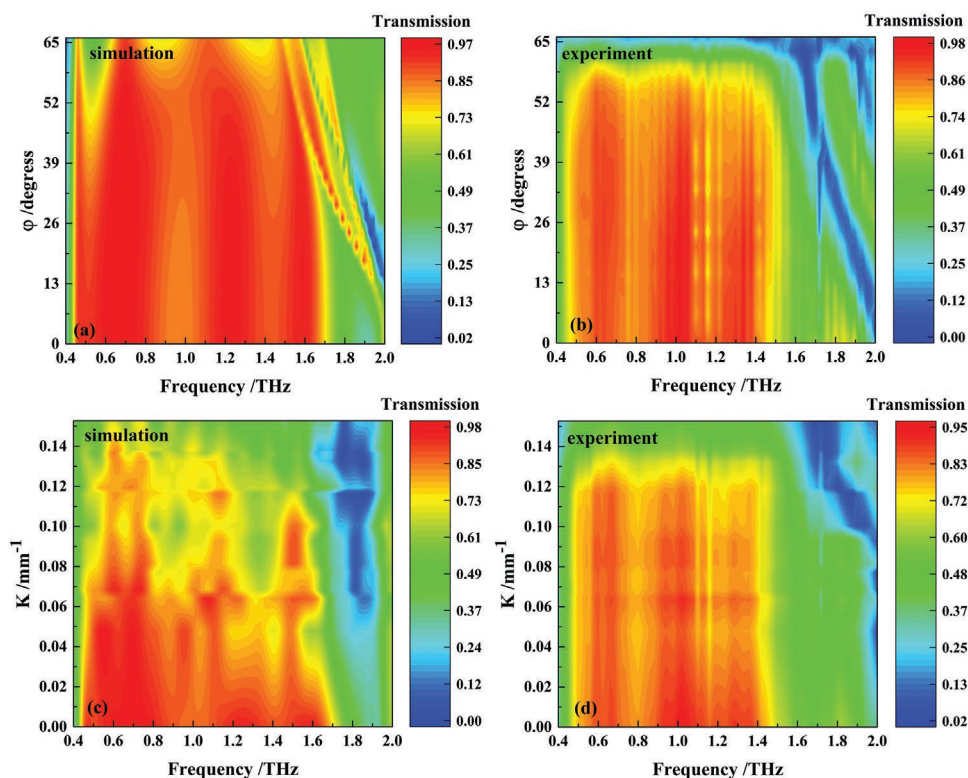


**Figure 5.** Effects of wide-angle oblique incidence and structural bending on transmission. a, b) Simulated and measured transmission spectra of cross-polarized waves when the azimuth  $\varphi$  changes gradually from  $0^\circ$  to  $65^\circ$ . c, d) Simulated and measured transmission spectra of cross-polarized waves when the curvature  $K$  changes gradually from 0 to  $0.14 \text{ mm}^{-1}$ .

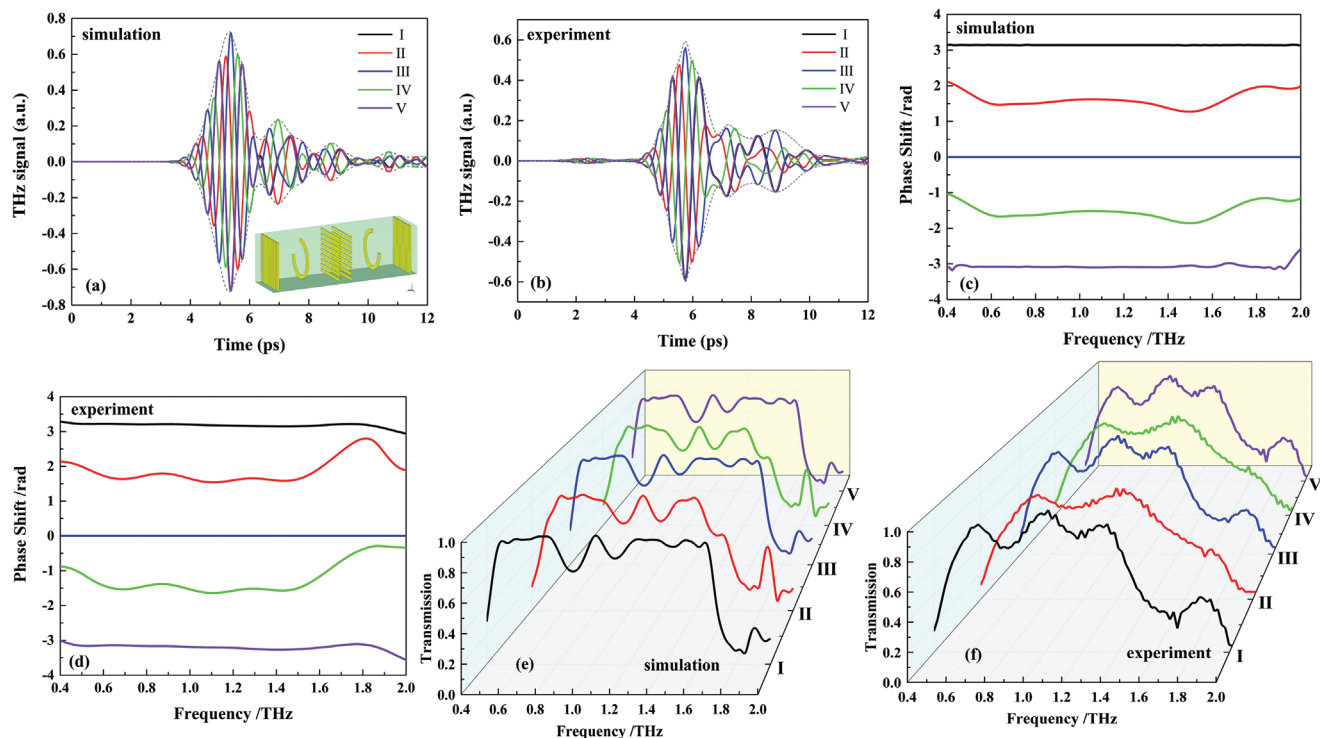


**Figure 6.** Temporal waveforms, phase shift, and transmission spectra of co-polarized waves. a, b) Simulated and measured temporal waveforms. Insets: the unit cell of the array, which consists of subunit A and subunit B. c, d) Phase shift spectra obtained by FT of temporal waveforms shown in (a) and (b), respectively. e, f) Transmission spectra obtained by FT of temporal waveforms shown in (a) and (b), respectively.

of subunit B only converts cross-polarized wave into co-polarized wave, but does not change the introduced phase shift between subunit A of different arrays. This means that the temporal waveform of the incident wave can be directly changed with different arrays. Consequently, the total current amplitude and direction may be set by varying the CEP of the THz pulse when the sample serves the THz-STM. Figure 6c,d shows the simulated and measured phase shift spectra, respectively, converting the CEP shift value from  $\pi$  to  $-\pi$ . The simulated and measured transmission spectra are plotted in Figure 6e,f, which show that subunit B will not induce large transmission loss. However, the larger transmission loss at high frequencies in the experiment may be caused by the mismatch between subunit A and subunit B during the bonding process.

## 4. Conclusion

In conclusion, we designed and experimentally demonstrated an ultra-thin and flexible CEP shifter, which can efficiently modulate the CEP of THz pulses. The CEP shift was realized by the resonance phase and Pancharatnam–Berry phase of SRR. Multi-beam interference was used to ensure high transmission, and the superposition of multiple resonance modes to expand the bandwidth of the spectrum. When the incident pulse was modulated by different stereo-MM arrays in turn, the change of temporal waveforms of the THz pulse was clearly observed using a THz-TDS. We also verify that the design is robust under wide angles of incidence and deformation of the sample. In addition, our design scheme can also be applied to other frequency bands by appropriately scaling the geometry parameters of the structure.

## 5. Experimental Section

**Numerical Simulations:** Full-wave electromagnetic simulations were carried out using FIT. In the modeling, the permittivity of Au was given by the Drude model with  $\epsilon_m = 1 - \omega_p^2 / (\omega(\omega + i\Gamma))$ , where plasma frequency  $\omega_p = 1.32 \times 10^{16}$  rad s<sup>-1</sup> and the collision frequency  $\Gamma = 1.2 \times 10^{14}$  rad s<sup>-1</sup>. The polyimide was modeled as a lossy dielectric with a dielectric constant  $\epsilon_p = 3.0 + 0.03i$ .<sup>[40]</sup> Periodic boundary conditions were set to the *x*- and *y*-boundaries and an open boundary condition was applied in the *z*-direction. The model was excited by a plane wave in the  $-z$ -direction and the probe was set in the  $+z$  direction to record far-field THz temporal waveforms.

**Optical Measurements:** In the experiment, a commercial THz-TDS system was used to characterize the performance of the sample. The sample was fixed on a micro-displacement stage and placed at the focus part of the THz beam path. By moving the sample, the THz pulse would pass through different MM arrays. All the measurements were carried out at room temperature in a dry air atmosphere to eliminate the disturbance from water vapor (humidity below 10%).

## Acknowledgements

This work was supported by the National Natural Science Foundation of China (61988102).

## Conflict of Interest

The authors declare no conflict of interest.

## Data Availability Statement

The data that support the findings of this study are available from the corresponding author upon reasonable request.

## Keywords

carrier-envelope phase, carrier-envelope phase shifter, metamaterials, temporal waveforms, terahertz

Received: March 8, 2022

Revised: April 23, 2022

Published online:

- [1] P. Michel, W. Benz, D. C. Richardson, *Nature* **2003**, 421, 608.
- [2] J. Zheng, E. Qiu, Y. Yang, Q. Lin, *Phys. Rev. A* **2012**, 85, 013417.
- [3] T. Rathje, A. M. Saylor, S. Zeng, P. Wustelt, H. Figger, B. D. Esry, G. G. Paulus, *Phys. Rev. Lett.* **2013**, 111, 093002.
- [4] H. Li, V. A. Sautenkov, Y. V. Rostovtsev, M. M. Kash, P. M. Anisimov, G. R. Welch, M. O. Scully, *Phys. Rev. Lett.* **2010**, 104, 103001.
- [5] H. Hirori, A. Doi, F. Blanchard, K. Tanaka, *Appl. Phys. Lett.* **2011**, 98, 091106.
- [6] M. Hohenleutner, F. Langer, O. Schubert, M. Knorr, U. Huttner, S. W. Koch, M. Kira, R. Huber, *Nature* **2015**, 523, 572.
- [7] K. N. Egodapitiya, S. Li, R. R. Jones, *Phys. Rev. Lett.* **2014**, 112, 103002.
- [8] T. L. Cocker, V. Jelic, M. Gupta, S. J. Molesky, J. A. J. Burgess, G. D. L. Reyes, L. V. Titova, Y. Y. Tsui, M. R. Freeman, F. A. Hegmann, *Nat. Photonics* **2013**, 7, 620.
- [9] T. L. Cocker, D. Peller, P. Yu, J. Repp, R. Huber, *Nature* **2016**, 539, 263.
- [10] K. Yoshioka, I. Katayama, Y. Minami, M. Kitajima, S. Yoshida, H. Shigekawa, J. Takeda, *Nat. Photonics* **2016**, 10, 762.
- [11] V. Jelic, K. Iwaszczuk, P. H. Nguyen, C. Rathje, G. J. Hornig, H. M. Sharum, J. R. Hoffman, M. R. Freeman, F. A. Hegmann, *Nat. Phys.* **2017**, 13, 591.
- [12] K. Yoshioka, I. Katayama, Y. Arashida, A. Ban, Y. Kawada, K. Konishi, H. Takahashi, J. Takeda, *Nano Lett.* **2018**, 18, 5198.
- [13] S. Yoshida, H. Hirori, T. Tachizaki, K. Yoshioka, Y. Arashida, Z.-H. Wang, Y. Sanari, O. Takeuchi, Y. Kanemitsu, H. Shigekawa, *ACS Photonics* **2019**, 6, 1356.
- [14] D. Peller, C. Roelcke, L. Z. Kastner, T. Buchner, A. Neef, J. Hayes, F. Bonafé, D. Sidler, M. Ruggenthaler, A. Rubio, R. Huber, J. Repp, *Nat. Photonics* **2020**, 15, 143.
- [15] M. Muller, N. M. Sabanes, T. Kampfrath, M. Wolf, *ACS Photonics* **2020**, 7, 2046.
- [16] S. Yoshida, Y. Arashida, H. Hirori, T. Tachizaki, A. Taninaka, H. Ueno, O. Takeuchi, H. Shigekawa, *ACS Photonics* **2021**, 8, 315.
- [17] S. E. Ammerman, V. Jelic, Y. Wei, V. N. Breslin, M. Hassan, N. Everett, S. Lee, Q. Sun, C. A. Pignedoli, P. Ruffieux, R. Fasel, T. L. Cocker, *Nat. Commun.* **2021**, 12, 6794.
- [18] M. Abel, D. M. Neumark, S. R. Leone, T. Pfeifer, *Laser Photonics Rev.* **2011**, 5, 352.
- [19] S.-W. Huang, G. Cirmi, J. Moses, K.-H. Hong, S. Bhardwaj, J. R. Birge, L.-J. Chen, E. Li, B. J. Eggleton, G. Cerullo, F. X. Kärtner, *Nat. Photonics* **2011**, 5, 475.
- [20] W. P. Putnam, R. G. Hobbs, P. D. Keathley, K. K. Berggren, F. X. Kärtner, *Nat. Phys.* **2016**, 13, 335.
- [21] D. J. Jones, S. A. Diddams, J. K. Ranka, A. Stentz, R. S. Windeler, J. L. Hall, S. T. Cundiff, *Science* **2000**, 288, 635.
- [22] T. Fuji, A. Apolonski, F. Krausz, *Opt. Lett.* **2004**, 29, 632.
- [23] Y. Kawada, T. Yasuda, H. Takahashi, *Opt. Lett.* **2016**, 41, 986.

- [24] Q. Song, H. Chen, M. Zhang, L. Li, J. Yang, P. Yan, *APL Photonics* **2021**, *6*, 056103.
- [25] G. Liang, X. Hu, X. Yu, Y. Shen, L. H. Li, A. G. Davies, E. H. Linfield, H. K. Liang, Y. Zhang, S. F. Yu, Q. J. Wang, *ACS Photonics* **2015**, *2*, 1559.
- [26] K. Tang, K. Dong, J. Li, M. P. Gordon, F. G. Reichertz, H. Kim, Y. Rho, Q. Wang, C.-Y. Lin, C. P. Grigoropoulos, A. Javey, J. J. Urban, J. Yao, R. Levinson, J. Wu, *Science* **2021**, *374*, 1504.
- [27] Y. Li, C. T. Chan, E. Mazur, *Light Sci. Appl.* **2021**, *10*, 203.
- [28] S. Qu, Y. Hou, P. Sheng, *Proc. Natl. Acad. Sci. USA* **2021**, *118*, e2110490118.
- [29] S. Lee, W. T. Kim, J. H. Kang, B. J. Kang, F. Rotermund, Q. H. Park, *ACS Appl. Mater. Interfaces* **2019**, *11*, 7655.
- [30] Y. Zhao, Y. Zhang, Q. Shi, S. Liang, W. Huang, W. Kou, Z. Yang, *ACS Photonics* **2018**, *5*, 3040.
- [31] Z. Han, S. Ohno, Y. Tokizane, K. Nawata, T. Notake, Y. Takida, H. Minamide, *Opt. Express* **2017**, *25*, 31186.
- [32] X. Zhao, U. Shah, O. Glubokov, J. Oberhammer, *IEEE Trans. Microw. Theory Tech.* **2021**, *69*, 3219.
- [33] H. Zeng, H. Liang, Y. Zhang, L. Wang, S. Liang, S. Gong, Z. Li, Z. Yang, X. Zhang, F. Lan, Z. Feng, Y. Gong, Z. Yang, D. M. Mittleman, *Nat. Photonics* **2021**, *15*, 751.
- [34] N. Yu, P. Genevet, M. A. Kats, F. Aieta, J.-P. Tetienne, F. Capasso, Z. Gaburro, *Science* **2011**, *334*, 333.
- [35] L. Cong, Y. K. Srivastava, H. Zhang, X. Zhang, J. Han, R. Singh, *Light Sci. Appl.* **2018**, *7*, 28.
- [36] Z. Liu, Z. Li, Z. Liu, J. Li, H. Cheng, P. Yu, W. Liu, C. Tang, C. Gu, J. Li, S. Chen, J. Tian, *Adv. Funct. Mater.* **2015**, *25*, 5428.
- [37] I. Yamada, K. Takano, M. Hangyo, M. Saito, W. Watanabe, *Opt. Lett.* **2009**, *34*, 274.
- [38] C. Menzel, C. Rockstuhl, F. Lederer, *Phys. Rev. A* **2010**, *82*, 053811.
- [39] D. Jalas, A. Petrov, M. Eich, W. Freude, S. Fan, Z. Yu, R. Baets, M. Popović, A. Melloni, J. D. Joannopoulos, M. Vanwolleghem, C. R. Doerr, H. Renner, *Nat. Photonics* **2013**, *7*, 579.
- [40] S. Liu, T. J. Cui, Q. Xu, D. Bao, L. Du, X. Wan, W. X. Tang, C. Ouyang, X. Y. Zhou, H. Yuan, H. F. Ma, W. X. Jiang, J. Han, W. Zhang, Q. Cheng, *Light Sci. Appl.* **2016**, *5*, e16076.